

Factors Governing the Behavior of Aqueous Methane in Narrow Pores

Anh Phan¹, David R. Cole², and Alberto Striolo¹

¹ University College London, Department of Chemical Engineering, Torrington Place, London, WC1E7JE, United Kingdom

² School of Earth Sciences, The Ohio State University, Columbus, Ohio 43210, USA

Abstract

All-atom equilibrium molecular dynamics simulations were employed to investigate the behavior of aqueous methane confined in 1 nm-wide pores obtained from different materials. Models for silica, alumina, and magnesium oxide were used to construct the slit-shaped pores. The results show that methane solubility in confined water strongly depends on the confining material, with silica yielding the highest solubility in the systems considered here. The molecular structure of confined water differs within the three pores, and density fluctuations reveal that the silica pore is effectively less ‘hydrophilic’ than the other two pores considered. Comparing the water fluctuation autocorrelation function to local diffusion coefficients of methane across the hydrated pores we observed a direct proportional coupling between methane and water dynamics. These simulation results help to understand the behavior of gas in water confined within narrow sub-surface formations, with possible implications for fluid transport.

* Author to whom correspondence should be addressed: a.striolo@ucl.ac.uk

1. Introduction

Water and aqueous mixtures have been popular research subjects due to their involvement in many chemical and biological processes [1-5]. In a recently developed important application, high-pressure water is used to stimulate subsurface formations in the practice of hydraulic fracturing. In this process the rock is fractured to increase gas and oil permeation [6]. Recent investigations [7] reported the low recovery of hydraulic fracture water during well clean-up and flow back operations, suggesting that large amounts of water remain trapped within the sub-surface formations. King [7] suggested that hydraulic fracturing water may also be trapped in micro-fractures and small pores caused by pressure release. Because water entrapment in the shale may affect the well productivity, understanding systems composed by water and volatile hydrocarbons under confinement could play a significant role in the design of hydraulic fracturing processes towards enhancing well performance and hydrocarbon recovery, and more in general could help us rationalizing the geochemical processes at Earth's subsurface and deep within the crust and mantle, which affect technologies such as carbon sequestration. It is known that structural and dynamical properties of confined water are strongly affected by the solid substrate characteristics, yielding different behaviors compared to those observed in the bulk [8]. Several attempts have been made to relate the behavior of water molecules near an interface to hydrophobic/philic features at sub-nanometer resolution. We explore here whether small changes in surface properties can yield marked differences in the effective hydrophobic vs. hydrophilic features of a narrow pore. The feature of interest is the methane solubility in confined water, which is directly related to hydraulic fracturing applications. In a recent contribution we reported that methane solubility in water increases significantly when water is confined in slit-shaped pores of width 1 nm carved out of silica [9]. This investigation will clarify whether the features of the confining material are essential for this observation, or instead if the pore size is the most important parameter. To quantify the molecular features of confined water we investigate its structure, and its density fluctuations, building on recent progress in the field [10-12].

In this study, we report equilibrium molecular dynamics (MD) simulations for methane – water mixtures confined within 1 nm slit-shaped nanopores in equilibrium with bulk methane. In addition to solubility

and structure, we also quantify the mobility of methane within the three pores of interest. The simulations are conducted at the temperature $T=300\text{K}$, and at bulk pressures P_{bulk} in the range from ~ 6 to 82 MPa. Silica, alumina, and magnesium oxide (MgO) were used as solid substrates because they are fundamental components of many minerals found in the subsurface. In the remainder of the article we first introduce the simulation methodology; we then discuss the results, i.e., methane solubility, fluid structure, density fluctuations, and mobility; we finally summarize our main results.

2. Simulation Methodology

Aqueous methane confined in silica, alumina, and MgO narrow pores was studied by all atom molecular dynamics (MD) simulations using the package GROMACS [13, 14][13, 14]. Two slabs of each type of pore material facing each other across the pore volume along the Z direction yield slit-shaped pores. The silica slabs were constructed to reproduce β -cristobalite SiO_2 [9, 15-17]. Alumina pore surfaces were modeled as crystallographic faces of sapphire $\alpha\text{-Al}_2\text{O}_3$ (space group $R\bar{3}c$), C plane (0001) [18, 19]. Each MgO slab was derived from the space group $Fm\bar{3}m$ along the (001) plane [20, 21]. All the non-bridging oxygen atoms on the silica and alumina surfaces were protonated, while the MgO surfaces were not hydroxylated, as suggested by theoretical and experimental observations[16, 17, 22]. In a prior simulation we detailed the behavior of pure water supported on free-standing solid surfaces obtained from these three model materials [23]. Each of the two surfaces placed parallel to the X-Y plane of the simulation box and across the pore volume is of dimensions 104.05×100.8 , 91.35×90.68 , and 103×105.1 \AA^2 for the systems of silica, alumina, and MgO, respectively. The simulation box is periodic in the three directions. The Y dimension of the simulation boxes reflects the periodicity of the solid crystalline substrate; the X and Z dimensions were set to $224.78 \text{ \AA} - 42.92 \text{ \AA}$, $180.43 \text{ \AA} - 33.82 \text{ \AA}$ and $185.1 \text{ \AA} - 33.12 \text{ \AA}$ for silica, alumina and MgO systems, respectively. All simulations were carried out for pores of width 10 \AA (the pore width refers to the shortest center-to-center distance between surface oxygen atoms of the solid slabs across the pore volume). Due to periodic boundary conditions, the nanopores are

effectively infinite along the Y direction. On the contrary, the pores are finite along the X direction, along which they are exposed to “bulk” systems. The simulation setup mimics the one implemented in our previous study [9].

The initial configurations for the three systems are built with water and methane molecules placed outside the slit pore, in the bulk region. As the simulation progresses, water and methane fill both the pore and the bulk volume. The number of methane molecules was varied from 1000 to 4000 while the number of water molecule was fixed at 3300, 1000 and 1500 for the silica, alumina, and MgO systems, respectively. These different amounts of water molecules were chosen because they were sufficient to fill approximately half of the pore volume along the X direction. By changing the number of methane molecules we manipulated the bulk pressure, which we estimated for each system after equilibrium was achieved, using the Peng-Robinson equation of state from the pure methane density of molecules in the bulk gas phase [24]. The calculated bulk pressures for various CH₄-H₂O system compositions are shown in Table 1.

Table 1. Bulk phase pressure estimated for seven methane-water systems simulated at T=300K.

System Composition	Estimated Bulk Pressure (MPa)		
	Silica (3300 H ₂ O)	Alumina (1000 H ₂ O)	Magnesium Oxide (1500 H ₂ O)
1000 CH ₄	6.3	9.3	9.6
1500 CH ₄	9.3	14.7	14.9
2000 CH ₄	12.2	21.4	21.2
2500 CH ₄	15.2	29.8	28.9
3000 CH ₄	18.9	41.7	40.0
3500 CH ₄	22.8	58.2	55.0
4000 CH ₄	27.6	82.4	76.1

The CLAYFF force field was implemented to describe the three narrow pores [25]. Silicon, aluminum and oxygen atoms were held at fixed positions while the surface hydrogen atoms of the –OH groups were allowed to vibrate; all atoms in the MgO substrate were kept rigid. **At the simulated conditions (P up to 80 MPa and ambient T) many studies reported no significant structural distortions within the substrates considered here until pressures exceeding 10’s of GPa are reached [26-33]. We therefore consider it**

reasonable to maintain the pore models rigid (except for –OH vibrations) in our simulations. The optimized potential for liquid simulation in the united atom form (OPLS-UA) was implemented to model methane [34] and the rigid SPC/E model was used to simulate water [35]. The SPC/E water bonds and angles were kept fixed by employing the SETTLE algorithm [36]. Non-bonded interactions were modeled by means of dispersive and electrostatic forces. The electrostatic interactions were modeled by the Coulombic potential. Dispersive interactions were modeled with 12-6 Lennard-Jones (LJ) potentials. The LJ parameters for unlike interactions were determined by the Lorentz-Berthelot mixing rules [37] from the values of like components. The cutoff distance for all interactions was set to 9 Å. Long-range corrections to electrostatic interactions were treated using the particle mesh Ewald (PME) method [38].

All simulations were performed in the canonical ensemble (NVT) where the number of particles (N), the simulation volume (V), and the temperature (T) were kept constant. The simulated temperature was maintained at 300 K controlled by Nose-Hoover thermostat [39, 40] with a relaxation time of 100 fs. The equations of motion were solved by implementing the leapfrog algorithm [41] with 1.0 fs time steps. The total simulation time was 49 ns. Data analysis was conducted over the last 2 ns of the simulations, after 47 ns of equilibration were completed. Equilibration was considered achieved when the density of methane within the pore approached a constant value that did not change appreciably over 13 ns.

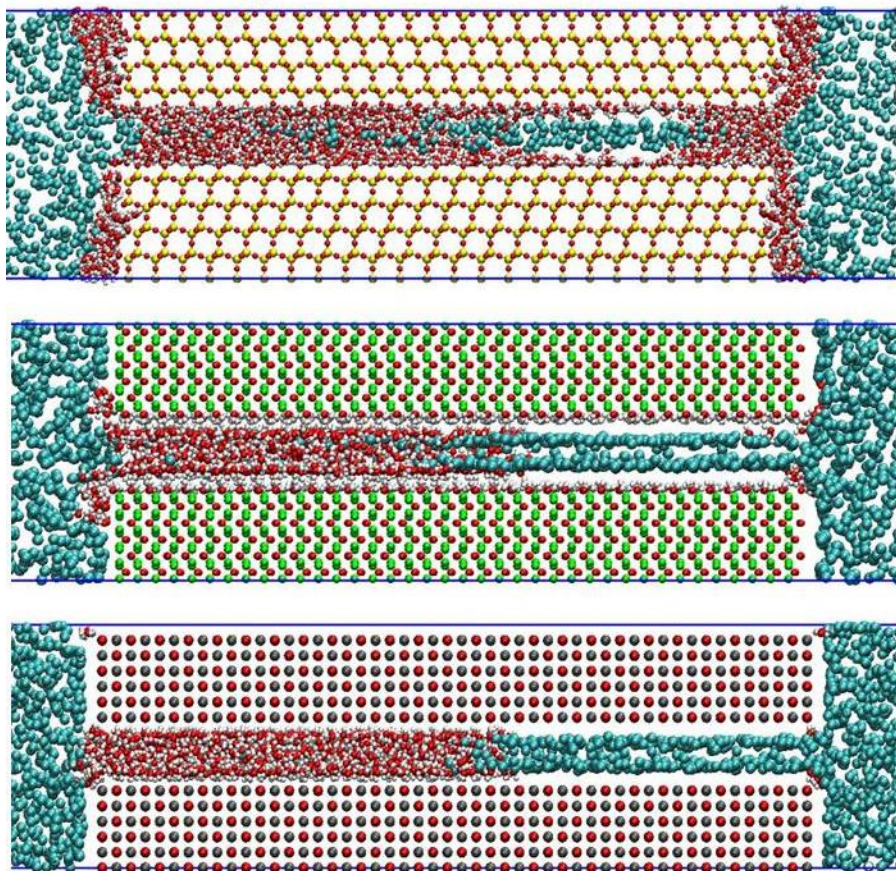


Figure 1. Representative simulation snapshots for aqueous methane in slit-shaped silica (top panel), alumina (middle panel) and MgO (bottom panel) pores of width 1.0 nm. Red, white, cyan, yellow, green and gray spheres represent oxygen, hydrogen, methane, silicon, aluminum and magnesium atoms, respectively.

3. Results and Discussion

Methane Solubility

The final configurations obtained for aqueous methane confined in the silica (top), alumina (middle) and MgO (bottom) pores at 300K after 49 ns are shown in Figure 1. For all simulated systems water occupies approximately half of the pore volume, and methane occupies the remainder of the pore and most of the bulk. Similar to the systems confined in our previous study [9], focused on silica pores, an interface is observed between the water-rich and the methane-rich phases within the alumina and MgO pores. We identify as Region I the pore volume occupied mostly by water with methane dissolved in it (left in Figure 1); Region II is the pore volume occupied mostly by methane (right in Figure 1). A significant

difference in the distribution of water and methane in Region II within the three pores is observed: within the silica pore water wets the surfaces and methane occupies the pore center, while in alumina and MgO pores only methane molecules occupy the whole Region II. Water at contact with the silica surface within Region II is able to form hydrogen bonds with the surface –OH groups available on this substrate, as described elsewhere [23]. This is not possible on the other two substrates, where the density of adsorption sites is too large (i.e., while the density of –OH groups is 4.54 per nm² on silica, the surface density of OH groups is of 15 per nm² on alumina and the surface density of Mg atoms is of 14 per nm² on the MgO substrate). The Region I – Region II interface that can be seen roughly parallel to the Y direction of the simulation box is irregular in shape (not shown for brevity). The irregularity of the Region I – Region II interface, the presence of water molecules on the pore opening from Region II to the bulk system, and the presence of water molecules near the silica surface cause the methane molecules confined in Region II of the silica pore in Figure 1 to appear disordered. While the methane distribution would change with variations in the amount of water simulated in this system, as well as upon variations in pore width, we have not varied the size of the simulation box in this investigation.

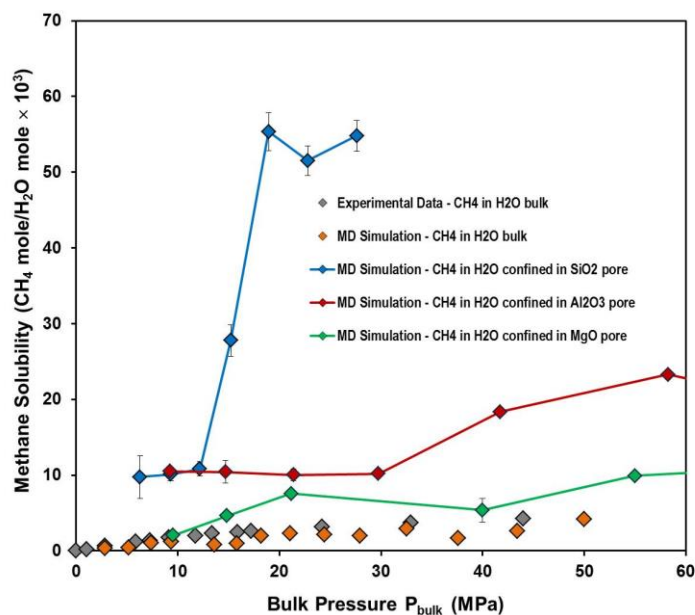


Figure 2. Methane solubility in confined water as a function of bulk pressure. Simulation data for aqueous CH₄ confined in silica, alumina, and MgO pores are shown as blue, red, and green diamonds, respectively. Lines are guides to the eye. Simulated bulk CH₄ solubility data in liquid water at 298K as reported by Sakamaki et al. [42] are shown as orange diamonds. The corresponding experimental data for CH₄ in bulk water [43-45] are shown as gray diamonds.

Following our prior work [9], we computed the methane solubility in the confined water within Region I in the three pores. It is worth repeating that for these calculations we only consider the water-methane mixture in Region I. The results are shown in Figure 2, in which methane solubility is shown as a function of bulk pressure. The bulk pressure is estimated from the methane density using an equation of state (see Table 1). The blue, red, and green symbols are the results of methane solubility in water confined in silica, alumina, and MgO pores at 300K. We also report the methane solubility in bulk liquid water at 298 K as predicted, using simulations, by Sakamaki et al. [42] (orange symbols) as well as the correspondent experimental data from literature [43-45] (gray symbols). The results in Figure 2 are consistent with a significant increase of methane solubility in water due to confinement. The enhancement of methane solubility is likely due, in part, to the enhanced pressure in the pore. However, as we discussed in our previous work [9], this increased pressure is not sufficient to explain the high solubility predicted in confinement. Comparing the methane solubility in confined water within the three pores, we observe that

the results obtained in the silica pore are much higher than those found within the alumina and MgO pores, with the results obtained in the MgO pores showing the lowest solubility out of the three confined systems considered. In addition to differences in pressures within the pores, it is also possible that the distinct structure of confined water within the three pores is responsible for the results observed. We also note that the methane solubility estimated from our simulations show large variations upon relatively small changes in bulk pressure. While we attribute these changes to statistical uncertainty, it is possible that other factors play important roles (e.g., the structure and the density fluctuations of confined water).

Structure of Confined Fluids - Methane and Water

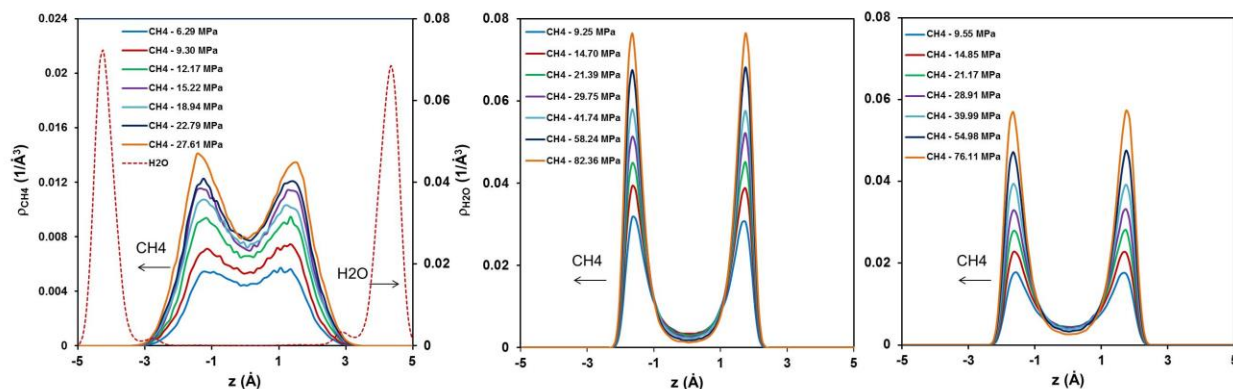


Figure 3. Density profiles of water oxygen atoms (dotted lines) and methane molecules (continuous lines) in Region II as a function of the distance z across the silica (left), alumina (middle), and MgO (right) pores. The results are obtained from seven simulation systems for each pore. The reference ($z=0$) corresponds to the center of the pore.

It is worth noting that the tangential pressure in the pore is directly proportional to the methane density in the pore, as discussed in previous studies [9, 46]. In Figure 3 we report the molecular density of methane in Region II along the direction perpendicular to the pore surface within the silica (left), alumina (middle), and MgO (right) pores as the bulk pressure increases. The reference ($z=0$) corresponds to the center of the pore. The results show that generally the increase of bulk pressure increases the molecular density of methane in Region II for all three pores. Comparing the methane density confined within three pores, we find that the methane densities in the silica pores are much smaller than those found in the alumina and

MgO pores, which indicates that the tangential pressures in the silica pore are also much smaller. However, the methane solubility in water confined in the silica pore is much higher than that found for the two other pores (see Figure 2). These results suggest that the differences in the methane solubility are probably related to the distinct structural behavior of confined water in the silica pore compared to the alumina and MgO pores. However, the higher methane solubility in water confined in the alumina pore than in the MgO pore is likely due to the higher tangential pressure, as suggested by the higher methane density in Region II (compare the data in middle and right panels in Figure 3 for systems at comparable bulk pressure). For completeness, we also report the water density profiles within the three pores. As mentioned above, water wets the silica surface, yielding a very dense molecular layer near the solid surfaces, while it is essentially not present within the other two pores considered here.

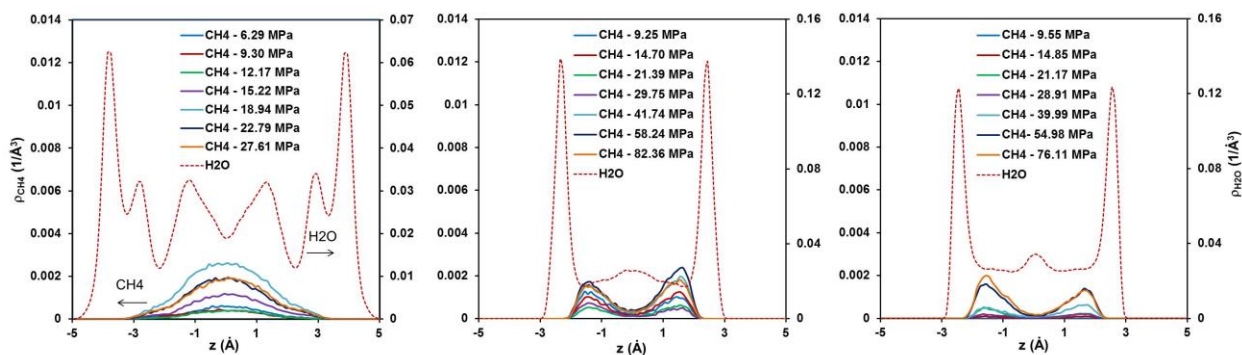


Figure 4. Density profiles of water oxygen atoms (dotted lines) and methane molecules (continuous lines) in Region I as a function of the distance z across the silica (left), alumina (middle), and MgO (right) pores. The results are obtained from seven simulation systems for each pore. The reference ($z=0$) corresponds to the center of the pore.

In Figure 4 we present the methane density profiles within Region I for the three pores considered as a function of bulk pressure. Generally the molecular density of methane in Region I increases as the bulk pressure increases. The results suggest that methane molecules are always excluded from the two hydration layers near the solid surfaces in all hydrated pores; while methane molecules accumulate in a rather wide region near the center of the silica pore, they yield two layers off-center of alumina and MgO

pores. For completeness, we also report the density profiles for water in the same region. The results for the density profiles of water oxygen atoms within Region I for the three pores show that more well-defined hydration layers are observed in the silica pore compared to two other pores. It is worth pointing out that methane molecules always accumulate in correspondence of density minima identified by the water density profiles.

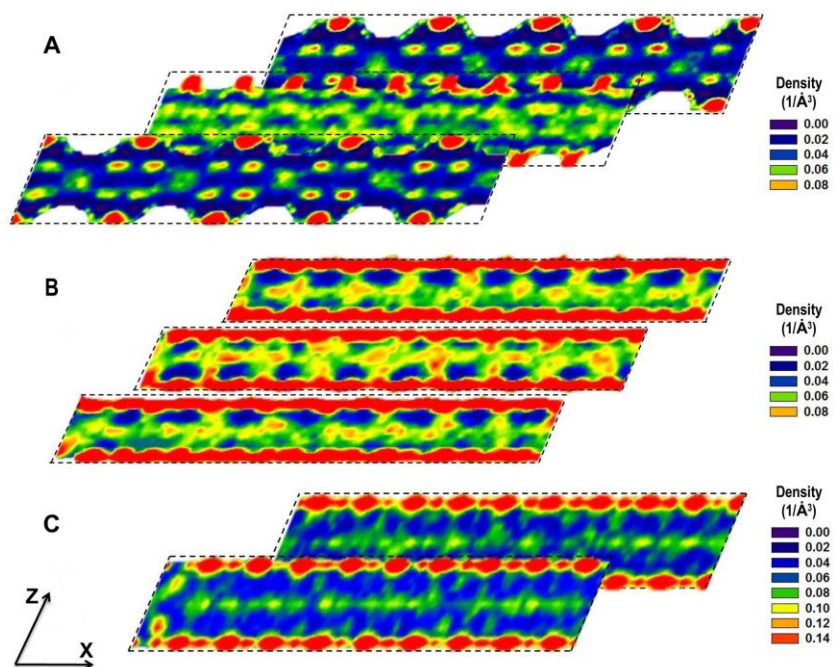


Figure 5. In-plane density distributions of water oxygen atoms found in layers parallel to the X – Z plane at several locations along the Y direction within silica (panel A), alumina (panel B) and MgO (panel C) pores. The results are obtained from systems containing only water. Densities are expressed in number of molecules per cubic angstrom. The consecutive layers were located at the following positions along the Y direction: for the silica pore the three layers were from 3.75 Å to 4.75 Å, from 4.75 Å to 5.75 Å, and from 5.75 Å to 6.75 Å; for the alumina pore the three layers were from 10 Å to 12 Å, from 12 Å to 14 Å, and from 14 Å to 16 Å; for the MgO pore the two layers were from 9 Å to 11 Å and from 11 Å to 13 Å.

Analysis of the distributions of water molecules within three pores could allow us to gain better insights into the structure of confined water. We calculated the in-plane density distributions of water oxygen atoms found in layers parallel to the X – Z plane at several locations along the Y direction. In Figure 5 we

report the results obtained for silica (panel A), alumina (panel B) and MgO (panel C) pores. The results are obtained from systems containing water only. The high-density areas (red-green spots) of the contour plots indicate the positions where the water oxygen atoms preferentially reside. Visual inspection of the results suggests a significant difference in the structural properties of confined water. Specifically, water molecules spread on the silica surfaces yielding small volumes depleted of water (as seen in the panel A) while they fill the alumina and MgO pores thoroughly, forming two well-defined hydration layers in contact with the surfaces (panels B and C). These distributions indicate that cavities are stably formed only in the hydrated silica pore while they are not typically present in the other hydrated pores.

Water Density Fluctuations Under Confinement - Degree of Hydrophobicity

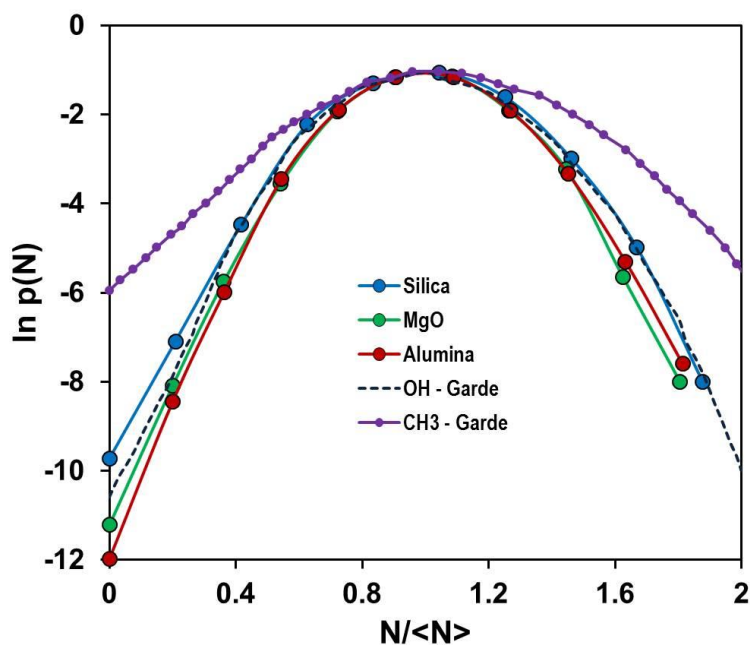


Figure 6. Probability distribution for observing N water molecules, $p(N)$, in a small spherical observation volume ($r = 3.3 \text{ \AA}$) located at the center of the hydrated silica (blue), alumina (red), and MgO (green) pores. The results are obtained from the systems containing only water in the nanopores. Results for observing N water molecules in the same probe volume next to hydrophilic OH (black dashed) and hydrophobic CH₃ (purple) surfaces reported by Garde et al. [11] are shown for comparison.

To quantify the differences in the behavior of confined water, which might result in differences in methane solubility, we quantify the **water density fluctuations** within the hydrated pores. Specifically, we **calculated** the probability of observing N molecules within a small spherical observation volume v of radius $r = 3.3 \text{ \AA}$ located at the center of the hydrated silica (blue), alumina (red), and MgO (green) pores. The probabilities are calculated as [12]:

$$P_v(N) = \langle \delta(N_v - N) \rangle = \lim_{t \rightarrow \infty} \frac{1}{t} \int_0^t dt' \delta(N_v(t') - N) \quad (1)$$

Garde and coworkers [10] showed that the spontaneous formation of cavities within hydration water is a strong signature that discriminates among surfaces of different degrees of hydrophobicity. Other quantities such as local averaged water density and contact angle do not seem sufficient to provide such a discriminant [23]. In Figure 6 we show the results for the calculations of Eq. (1) within the three hydrated pores considered here. The results are compared to similar calculations reported in the literature for water on free-standing surfaces of varying degrees of hydrophobicity. Comparing the data, we observe that the three pores considered in this work can be considered ‘hydrophilic’; however, there is a clear difference in their relative degree of hydrophilicity, with the silica pores being less ‘hydrophilic’ than the other two pores considered. This observation could explain why methane is more favorably adsorbed within the hydrated silica pore than in the other two pores. Comparing the results obtained for the alumina with those found for MgO pores, we notice that the alumina pore is slightly more ‘hydrophilic’ than the MgO pore. This does not agree with the slightly larger methane solubility observed in water confined in the alumina vs. the MgO pore. In this case, the differences in tangential pressure, suggested by the differences in methane densities in Region II (see Figure 3) seem to be responsible for the differences in methane solubility. Garde et al. [11] stated that one important and direct consequence of enhanced fluctuations at an interface is that the formation of a cavity near that interface is easier. The results of the water distributions within the three pores reported in Figure 5 indeed confirm the observation of cavity formation within the hydrated silica pores while we do not see the cavities in the two other hydrated pores.

Coupling of Methane Dynamics to Hydration Fluctuations

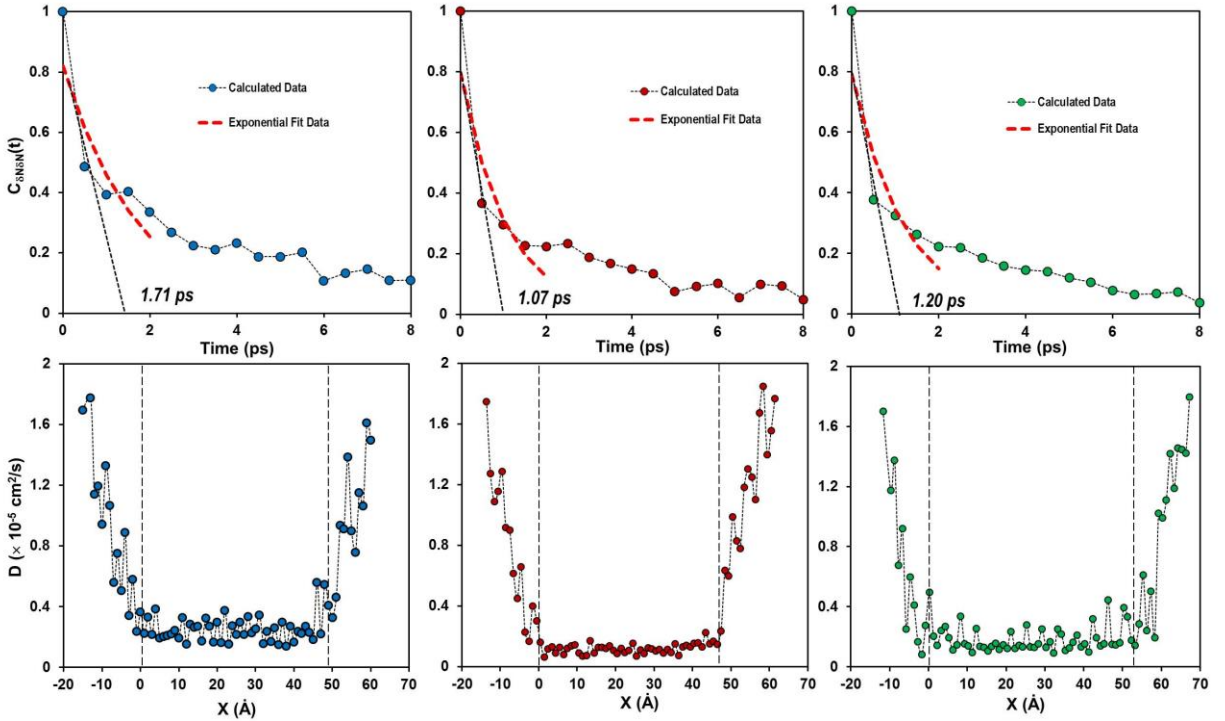


Figure 7. (Top) Normalized water fluctuation autocorrelation function $C_{\delta N \delta N}(t)$ in the silica (left), alumina (middle), and MgO (right) pores. The results are obtained from systems containing only water. (Bottom) Diffusion profiles for methane across the hydrated silica (left), alumina (middle), and MgO (right) pores. The results were obtained from the systems containing water fully occupying the pores and one methane molecule constrained at the center of the simulation box in Y-Z plane while it moves along the X direction. The region between two dashed lines represents the inner hydrated pore.

To further quantify the mutual relation between methane behavior and confined water properties, we analyzed the normalized water fluctuation autocorrelation function $C_{\delta N \delta N}(t)$ within the three pores and the methane diffusion profiles inside the hydrated pores. The results are shown in the top and bottom panels of Figure 7, respectively, for silica (left panels), alumina (middle panels) and MgO (right panels) pores. We computed the normalized water fluctuation autocorrelation function through the water occupancy $N(t)$ in the probe volume v ($r = 3.3 \text{ \AA}$) located at the center of the hydrated pores, defined as [47]:

$$C_{\delta N \delta N}(t) = \frac{\langle \delta N(t) \delta N(0) \rangle}{\langle \delta N(0) \delta N(0) \rangle} \quad \text{with } \delta N(t) = N(t) - \langle N \rangle \quad (2)$$

The local diffusion coefficients for methane were estimated from umbrella sampling trajectories according to a simplified form of the Woolf and Roux equation [48, 49]:

$$D(x = \langle x \rangle) = \frac{\text{var}(x)}{\tau_x} \quad , \quad (3)$$

where $\langle x \rangle$ is the average position of the harmonically restrained methane molecule along the X direction, $\text{var}(x) = \langle x^2 \rangle - \langle x \rangle^2$ is its variance, and τ_x is its correlation time, formally defined as

$$\tau_x = \frac{\int_0^\infty \langle \delta x(t) \delta x(0) \rangle dt}{\langle \delta x^2 \rangle} \quad \text{with } \delta x(t) = x(t) - \langle x \rangle \quad (4)$$

For the diffusion calculations, the methane molecule is forced to remain at the center of the simulation box in the Y-Z plane while it moves along the X direction. The $x = 0$ is located at the pore entrance.

From single exponential fits on the normalized water fluctuation autocorrelation function we find that the decay time of water fluctuations in the three pores decreases in the order silica (~ 1.71 ps), MgO (~ 1.20 ps) and alumina pore (~ 1.07 ps). This means that the hydration fluctuation in the pore increases in the order alumina < MgO < silica pore, which is consistent with the density fluctuation results in Figure 6.

Note that the exponential fitting to the autocorrelation functions is only conducted at short observation times (less than 2 ps), where a single exponential function is assumed to be sufficient to capture the system behaviour. The decay time obtained for the normalized water fluctuation autocorrelation function next to hydrophilic surfaces is comparable to that reported for bulk water by Setny et al. [47]. Note that the characteristics of water density fluctuations next to hydrophilic surfaces are similar to those obtained for bulk water [11].

In the bottom panels of Figure 7, we show the diffusion profiles of the methane molecule across three hydrated pores. The estimated diffusion coefficients decrease as methane enters the hydrated pore. The calculated diffusion coefficient of methane outside the hydrated pores ($\sim 1.8 \times 10^{-5}$ cm²/s) is consistent with the experimental diffusivity of methane in bulk water at similar conditions (1.9×10^{-5} cm²/s) [50]. The results of averaged diffusion coefficients of methane inside the hydrated pores (the region between two dashed lines) suggest that methane diffuses faster in the hydrated silica pore ($\sim 2.45 \pm 0.03 \times 10^{-6}$

cm²/s) than in the alumina ($\sim 1.12 \pm 0.02 \times 10^{-6}$ cm²/s) and MgO ($\sim 1.61 \pm 0.03 \times 10^{-6}$ cm²/s) pores. Correlating the methane diffusion with the hydration fluctuations in the silica, alumina and MgO pores clearly indicates a direct proportional coupling between methane and water dynamics.

4. Conclusions

We employed molecular dynamics simulations to study the behavior of methane dissolved in water confined within silica, alumina, and MgO pores with 1 nm width. The methane solubility in confined water in the silica pore is much higher than that found in the two other pores at comparable T and P. This is due to the fact that the hydrated silica pore is less ‘hydrophilic’ than the other two pores considered. Despite the fact that the hydrated alumina pore is slightly more hydrophilic than the hydrated MgO pore, methane solubility in water confined in the alumina pore is slightly larger than that obtained in the MgO pore. This difference is probably due to higher tangential pressure expected in the alumina pore. Analysis of water fluctuation autocorrelation functions and local diffusion coefficients of methane across the hydrated pores shows a direct proportional coupling between methane and water dynamics. These results suggest that the properties of confined water are dictating both structural and dynamic behavior of methane dissolved in the hydrated pores. Implications in the diffusion of fluids in the sub-surface should be investigated in the framework of hydraulic fracturing, shale gas, and perhaps also carbon sequestration.

Acknowledgements

Generous allocations of computing time were provided by the University College London Research Computing Platforms Support (LEGION), the Oklahoma Supercomputing Center for Education and Research (OSCER) and the National Energy Research Scientific Computing Center (NERSC) at Lawrence Berkeley National Laboratory. NERSC is supported by the DOE Office of Science under Contract No. DE-AC02-05CH11231. Ms. Anh Phan wishes to thank financial support from the Sloan Foundation, via the Deep Carbon Observatory. DRC was

supported by the Department of Energy, Office of Basic Energy Sciences, Geosciences program under grant DE-SC0006878. AS acknowledges partial financial support from a Marie Curie Career Initiation Grant.

References

1. Fornasiero F, Park HG, Holt JK, Stadermann M, Grigoropoulos CP, Noy A, Bakajin O. 2008 Ion exclusion by sub-2-nm carbon nanotube pores. *P Natl Acad Sci USA* **105**, 17250-17255. (doi: 10.1073/pnas.0710437105)
2. Jiang YX, Lee A, Chen JY, Cadene M, Chait BT, MacKinnon R. 2002 Crystal structure and mechanism of a calcium-gated potassium channel. *Nature* **417**, 515-522. (doi: 10.1038/417515a)
3. Argyris D, Cole DR, Striolo A. 2010 Ion-Specific Effects under Confinement: The Role of Interfacial Water. *Acs Nano* **4**, 2035-2042. (doi: 10.1021/Nn100251g)
4. Ho TA, Argyris D, Cole DR, Striolo A. 2012 Aqueous NaCl and CsCl Solutions Confined in Crystalline Slit-Shaped Silica Nanopores of Varying Degree of Protonation. *Langmuir* **28**, 1256-1266. (doi: 10.1021/La2036086)
5. Hille B. 2001 *Ion Channels of Excitable Membranes*. Sunderland, MA: Sinauer Associates.
6. Yethiraj A, Striolo A. 2013 Fracking: What Can Physical Chemistry Offer? *J Phys Chem Lett* **4**, 687-690. (doi: 10.1021/Jz400141e)
7. King GE. 2012 Hydraulic Fracturing 101: What Every Representative, Environmentalist, Regulator, Reporter, Investor, University Researcher, Neighbor and Engineer Should Know About Estimating Frac Risk and Improving Frac Performance in Unconventional Gas and Oil Wells. SPE Hydraulic Fracturing Technology Conference, February 6-8, The Woodlands, Texas, U.S.A pp 1-80.
8. Striolo A. 2011 From Interfacial Water to Macroscopic Observables: A Review. *Adsorpt Sci Technol* **29**, 211-258. (doi: 10.1260/0263-6174.29.3.211)
9. Phan A, Cole DR, Striolo A. 2014 Aqueous Methane in Slit-Shaped Silica Nanopores: High Solubility and Traces of Hydrates. *J Phys Chem C* **118**, 4860-4868. (doi: 10.1021/Jp500081t)
10. Godawat R, Jamadagni SN, Garde S. 2009 Characterizing hydrophobicity of interfaces by using cavity formation, solute binding, and water correlations. *P Natl Acad Sci USA* **106**, 15119-15124. (doi: 10.1073/pnas.0902778106)
11. Jamadagni SN, Godawat R, Garde S. 2011 Hydrophobicity of Proteins and Interfaces: Insights from Density Fluctuations. *Annu Rev Chem Biomol* **2**, 147-171. (doi: 10.1146/annurev-chembioeng-061010-114156)
12. Limmer DT, Willard AP, Madden P, Chandler D. 2013 Hydration of metal surfaces can be dynamically heterogeneous and hydrophobic. *P Natl Acad Sci USA* **110**, 4200-4205. (doi: 10.1073/pnas.1301596110)
13. Hess B, Kutzner C, van der Spoel D, Lindahl E. 2008 GROMACS 4: Algorithms for Highly Efficient, Load-Balanced, and Scalable Molecular Simulation. *Journal of Chemical Theory and Computation* **4**, 435-447. (Doi 10.1021/Ct700301q)
14. Van der Spoel D, Lindahl E, Hess B, Groenhof G, Mark AE, Berendsen HJC. 2005 GROMACS: Fast, flexible, and free. *J Comput Chem* **26**, 1701-1718. (doi: 10.1002/Jcc.20291)
15. Ho TA, Argyris D, Papavassiliou DV, Striolo A, Lee LL, Cole DR. 2011 Interfacial water on crystalline silica: a comparative molecular dynamics simulation study. *Mol Simulat* **37**, 172-195. (doi: 10.1080/08927022.2010.513008)
16. Argyris D, Tummala NR, Striolo A, Cole DR. 2008 Molecular structure and dynamics in thin water films at the silica and graphite surfaces. *J Phys Chem C* **112**, 13587-13599. (doi: 10.1021/Jp803234a)

17. Argyris D, Cole DR, Striolo A. 2009 Hydration Structure on Crystalline Silica Substrates. *Langmuir* **25**, 8025-8035. (doi: 10.1021/la9005136)
18. Argyris D, Ho TA, Cole DR, Striolo A. 2011 Molecular Dynamics Studies of Interfacial Water at the Alumina Surface. *J Phys Chem C* **115**, 2038-2046. (doi: 10.1021/Jp109244c)
19. Phan A, Cole DR, Striolo A. 2014 Preferential Adsorption from Liquid Water-Ethanol Mixtures in Alumina Pores. *Langmuir* **30**, 8066-8077. (doi: 10.1021/La501177t)
20. Causa M, Dovesi R, Pisani C, Roetti C. 1986 Abinitio Hartree-Fock Study of the MgO(001) Surface. *Surf Sci* **175**, 551-560. (doi: 10.1016/0039-6028(86)90012-9)
21. Scamehorn CA, Hess AC, Mccarthy MI. 1993 Correlation Corrected Periodic Hartree-Fock Study of the Interactions between Water and the (001) Magnesium-Oxide Surface. *J Chem Phys* **99**, 2786-2795. (doi: 10.1063/1.465187)
22. Refson K, Wogelius RA, Fraser DG, Payne MC, Lee MH, Milman V. 1995 Water chemisorption and reconstruction of the MgO surface. *Phys Rev B* **52**, 10823-10826. (doi: 10.1103/PhysRevB.52.10823)
23. Phan A, Ho TA, Cole DR, Striolo A. 2012 Molecular Structure and Dynamics in Thin Water Films at Metal Oxide Surfaces: Magnesium, Aluminum, and Silicon Oxide Surfaces. *J Phys Chem C* **116**, 15962-15973. (doi: 10.1021/Jp300679v)
24. Golebiowska M, Roth M, Firlej L, Kuchta B, Wexler C. 2012 The reversibility of the adsorption of methane-methyl mercaptan mixtures in nanoporous carbon. *Carbon* **50**, 225-234. (doi: 10.1016/j.carbon.2011.08.039)
25. Cygan RT, Liang JJ, Kalinichev AG. 2004 Molecular models of hydroxide, oxyhydroxide, and clay phases and the development of a general force field. *J Phys Chem B* **108**, 1255-1266. (doi: 10.1021/Jp0363287)
26. Huang LP, Durandurdu M, Kieffer J. 2006 Transformation pathways of silica under high pressure. *Nat Mater* **5**, 977-981. (doi: 10.1038/nmat1760)
27. Tsuchida Y, Yagi T. 1990 New Pressure-Induced Transformations of Silica at Room-Temperature. *Nature* **347**, 267-269. (doi: 10.1038/347267a0)
28. Coppari F, Smith RF, Eggert JH, Wang J, Rygg JR, Lazicki A, Hawreliak JA, Collins GW, Duffy TS. 2013 Experimental evidence for a phase transition in magnesium oxide at exoplanet pressures. *Nat Geosci* **6**, 926-929. (doi: 10.1038/NGEO1948)
29. Duffy TS, Hemley RJ, Mao HK. 1995 Equation of State and Shear-Strength at Multimegabar Pressures - Magnesium-Oxide to 227gpa. *Phys Rev Lett* **74**, 1371-1374. (doi: 10.1103/PhysRevLett.74.1371)
30. Jephcoat AP, Hemley RJ, Mao HK. 1988 X-Ray-Diffraction of Ruby (Al₂O₃-Cr³⁺) to 175 Gpa. *Physica B & C* **150**, 115-121. (doi: 10.1016/0378-4363(88)90112-X)
31. Funamori N, Jeanloz R. 1997 High-pressure transformation of Al₂O₃. *Science* **278**, 1109-1111. (doi: 10.1126/science.278.5340.1109)
32. Lin JF, Degtyareva O, Prewitt CT, Dera P, Sata N, Gregoryanz E, Mao HK, Hemley RJ. 2004 Crystal structure of a high-pressure/high-temperature phase of alumina by in situ X-ray diffraction. *Nat Mater* **3**, 389-393. (doi: 10.1038/nmat1121)
33. Thomson KT, Wentzcovitch RM, Bukowinski MST. 1996 Polymorphs of alumina predicted by first principles: Putting pressure on the ruby pressure scale. *Science* **274**, 1880-1882. (doi: 10.1126/science.274.5294.1880)
34. Jorgensen WL, Gao J. 1986 Monte-Carlo Simulations of the Hydration of Ammonium and Carboxylate Ions. *J Phys Chem-Us* **90**, 2174-2182. (doi: 10.1021/J100401a037)
35. Berendsen HJC, Grigera JR, Straatsma TP. 1987 The Missing Term in Effective Pair Potentials. *J Phys Chem-Us* **91**, 6269-6271. (doi: 10.1021/J100308a038)
36. Miyamoto S, Kollman PA. 1992 Settle - an Analytical Version of the Shake and Rattle Algorithm for Rigid Water Models. *J Comput Chem* **13**, 952-962. (doi: 10.1002/jcc.540130805)

37. Allen MP, Tildesley DJ. 2004 *Computer Simulation of Liquids*. Oxford, UK: Oxford University Press.
38. Essmann U, Perera L, Berkowitz ML, Darden T, Lee H, Pedersen LG. 1995 A Smooth Particle Mesh Ewald Method. *J Chem Phys* **103**, 8577-8593. (doi: 10.1063/1.470117)
39. Hoover WG. 1985 Canonical Dynamics - Equilibrium Phase-Space Distributions. *Phys Rev A* **31**, 1695-1697. (doi: 10.1103/PhysRevA.31.1695)
40. Nose S. 1984 A Molecular-Dynamics Method for Simulations in the Canonical Ensemble. *Mol Phys* **52**, 255-268. (doi: 10.1080/00268978400101201)
41. Hockney RW, Goel SP, Eastwood JW. 1974 Quiet High-Resolution Computer Models of a Plasma. *J Comput Phys* **14**, 148-158. (doi: 10.1016/0021-9991(74)90010-2)
42. Sakamaki R, Sum AK, Narumi T, Ohmura R, Yasuoka K. 2011 Thermodynamic properties of methane/water interface predicted by molecular dynamics simulations. *J Chem Phys* **134**. (doi: 10.1063/1.3579480)
43. Culberson OL, Mcketta JJ. 1951 Phase Equilibria in Hydrocarbon-Water Systems .3. The Solubility of Methane in Water at Pressures to 10,000 Psia. *T Am I Min Met Eng* **192**, 223-226.
44. Yang SO, Cho SH, Lee H, Lee CS. 2001 Measurement and prediction of phase equilibria for water plus methane in hydrate forming conditions. *Fluid Phase Equilib* **185**, 53-63. (doi: 10.1016/S0378-3812(01)00456-3)
45. Chapoy A, Mohammadi AH, Richon D, Tohidi B. 2004 Gas solubility measurement and modeling for methane-water and methane-ethane-n-butane-water systems at low temperature conditions. *Fluid Phase Equilib* **220**, 113-121. (doi: 10.1016/j.fluid.2004.02.010)
46. Long Y, Palmer JC, Coasne B, Sliwinska-Bartkowiak M, Gubbins KE. 2011 Pressure enhancement in carbon nanopores: a major confinement effect. *Phys Chem Chem Phys* **13**, 17163-17170. (doi: 10.1039/C1cp21407a)
47. Setny P, Baron R, Kekenes-Huskey PM, McCammon JA, Dzubiella J. 2013 Solvent fluctuations in hydrophobic cavity-ligand binding kinetics. *P Natl Acad Sci USA* **110**, 1197-1202. (doi: 10.1073/pnas.1221231110)
48. Woolf TB, Roux B. 1994 Conformational Flexibility of O-Phosphorylcholine and O-Phosphorylethanolamine - a Molecular-Dynamics Study of Solvation Effects. *J Am Chem Soc* **116**, 5916-5926. (doi: 10.1021/Ja00092a048)
49. Hummer G. 2005 Position-dependent diffusion coefficients and free energies from Bayesian analysis of equilibrium and replica molecular dynamics simulations. *New J Phys* **7**. (doi: 10.1088/1367-2630/7/1/034)
50. Witherspoon PA, Saraf DN. 1965 Diffusion of Methane Ethane Propane and N-Butane in Water from 25 to 43 Degrees. *J Phys Chem-Us* **69**, 3752-3755. (doi: 10.1021/J100895a017)